Microchimica Acta (2020) 187: 588
https://doi.org/10.1007/s00604-020-04562-7

ORIGINAL PAPER

Molybdenum disulfide—gold nanoparticle nanocomposite in field-effect transistor back-gate for enhanced C-reactive protein detection

N. R. Dalila[1] · M. K. Md Arshad[1,2] · Subash C. B. Gopinath[1,3] · M. N. M Nuzaihan[1] · M. F. M. Fathil[1]

Received: 13 February 2020 / Accepted: 17 September 2020 / Published online: 5 October 2020

Abstract

Nanofabricated gold nanoparticles (Au-NPs) on MoS_2 nanosheets (Au-NPs/MoS_2) in back-gated field-effect transistor (BG-FET) are presented, which acts as an efficient semiconductor device for detecting a low concentration of C-reactive protein (C-RP). The decorated nanomaterials lead to an enhanced electron conduction layer on a 100-μm-sized transducing channel. The sensing surface was characterized by Raman spectroscopy, ultraviolet–visible spectroscopy (UV-Vis), atomic force microscopy (AFM), scanning electron microscopy (SEM), and high-power microscopy (HPM). The BG-FET device exhibits an excellent limit of detection of 8.38 fg/mL and a sensitivity of 176 nA/g·mL^{-1}. The current study with Au-NPs/MoS_2 BG-FET displays a new potential biosensing technology; especially for integration into complementary metal oxide (CMOS) technology for hand-held future device application.

Keywords C-reactive protein · Field-effect transistor · Gold nanoparticles · Molybdenum disulfide

Introduction

Cardiovascular diseases (CVD) are the principal cause of human death globally [1]. C-reactive protein (C-RP) has been widely studied as a diagnostic and indicative biomarker which is selected by experts to monitor cardiovascular disease attack and inflammation level in patients [2–4]. C-RP consists of a naturally ring-shaped structure and is well recognized as an acute-phase protein where it is synthesized by the liver [3]. The American Heart Association and the United States Centre for Disease Control had come-up with three C-RP concentration levels to monitor the elevation stages towards the cardiovascular risk: a C-RP concentration less than 1.0 μg/mL indicating a low-risk, while 1.0 to 2.0 μg/mL representing an average risk, and for above 3.0 μg/mL, it is representing a high-risk [4–6]. Consequently, a sensitive sensor to detect C-RP concentration as low as possible plays a crucial role in pharmaceutical and clinical studies [5]. As considered, preventing the lowest C-RP concentration level is better than curing at high-risk level.

The state-of-the-art in the semiconductor technologies integrated with nanomaterials has been enhanced tremendously compared with a few decades ago, in particular, two-dimensional (2D) nanomaterial transition-metal dichalcogenide (TMDs) [7]. Theoretically, MoS_2 is naturally existed as S-Mo-S, stacking with a trilayered chemical structure which is individually separated via weak Van der Waals force and found to be one of the most stable among 2D nanomaterials in TMDs [8]. MoS_2 also has a honeycomb configuration where the molybdenum atom is covalently sandwiched between two sulphur atoms [9, 10]. Higher sensitivity on the sensing surface with the integration of MoS_2 monolayers can be achieved upon interaction with various target biomolecules due to the atomically thin layer and sharp edge structures [11, 12]. Moreover, MoS_2 nanosheets are proudly known to have a large surface-to-volume ratio [13], biocompatibility, and non-toxic [14] and allow good electrical conductivity [15]. MoS_2 nanosheet incorporation has been

✉ M. K. Md Arshad
mohd.khairuddin@unimap.edu.my

[1] Institute of Nano Electronic Engineering, Universiti Malaysia Perlis, 01000 Kangar, Perlis, Malaysia

[2] School of Microelectronic Engineering, Universiti Malaysia Perlis, Pauh Putra, 02600 Arau, Perlis, Malaysia

[3] Faculty of Chemical Engineering Technology, Universiti Malaysia Perlis, 02600 Arau, Perlis, Malaysia

interestingly discovered by researchers in the field of electronic, electrochemical, and bioanalytical sensors [9, 16].

However, standalone MoS_2 deposition on the sensors is not strong enough to capture biological molecules due to their feeble interaction with MoS_2 [16]. Therefore, considerable attempts towards the hybridization of MoS_2 nanosheets with noble material, gold nanoparticles (Au-NPs) have been employed by several researchers to innovate the intrinsic property and absorption behaviour of materials [13, 15, 17, 18]. Au-NPs have the capability to adsorb molecules due to its broad surface free energy and excellent biocompatibility [19]. In addition, Au-NPs capably act as a defect marker for MoS_2 nanosheets layer, and it will construct selectively on defected MoS_2 edges by the non-covalent bonding, hence producing well-defined edge sites [20, 21]. Moreover, the location of sulphur (S) atom in the outer layer of MoS2 bonding is suitable for the metal ligand creation, providing strong Au–S bonds, thus improves the charge transfer between S and Au [15].

Several researches have reported the utilization of Au-NPs/MoS_2composite to enhance the biomolecules capturing performance for sensors. For instance, Sun et al. [14] developed a sandwich-type of an electrochemical immunoassay with the modification of MoS_2 nanosheets and Au-NPs with hybridization chain reaction on glassy carbon electrode (GCE) for the accurate quantitative insulin detection. The surface modification allows a large amount of antibody immobilization, thus demonstrating a good specificity and great sensitivity measurements due to the large surface area, leading to the acceleration of electron transfer movement on the GCE surface. Xu et al. [22] and Ma et al. [23] have reported high-performance detection using GCE-modified sensor with Au-NPs/MoS_2-graphene aerogel nanocomposite (GAs) and Au-NPs/MoS_2-reduced graphene oxide (rGO) nanocomposite, respectively, for the detection of prostate-specific antigen (PSA) [22], hydroquinone (HQ), catechol (CC), or resorcinol (RC) [23]. The interlayer spacers of MoS_2 effectively prevented the graphene from restacking, hence providing a good sensing surface to load more Au-NPS. The integration of MoS_2 with suitable functional materials endows a high catalysis effect for the electrochemical sensors [24].

Undoubtedly, the utilization of 2D graphene in electrochemical biosensors field has led to vast interest due to its fascinating properties [25]. However, there are reasons where MoS_2 is found to be more compatible in transistor over graphene (gapless) because of its capability to have large intrinsic bandgap [26]. A comparison of graphene and MoS_2 efficiency on label-free FET was demonstrated by Sarkar et al. [27]. MoS_2-based field-effect transistors were reported to surpass graphene-based sensors larger than 74-fold and to generate a more desirable outcome for bioassays [26, 27]. Graphene-based approach is not quite competent for the application in FET biosensors due to its lack of sensitivity and the ability to yield a low detection limit.

Despite Au-NPs/MoS_2 composite having a great prevalence and interest among researchers, yet there is no report for the fabrication of label-free Au-NPs/MoS_2-back-gated FET sensor for highly sensitive of C-RP detection. With regard to magnifying the sensitivity of the existing work, here reported a biosensor of gold nanoparticles/molybdenum disulfide-based back-gated field-effect transistor (Au-NPs/MoS2-BG-FET) for C-RP antigen detection. The back-gate biasing provides an excellent running current on a modified sensing channel to promote C-RP binding event. The idea of using MoS2 nanosheets on biomolecules sensing device was formed because of its large plane properties leading to a stable composition matter in liquid and gaseous states [28]. In this work, a *p*-type channel BG-FET is fabricated due to its excellent sensitivity compared with *n*-type channel [6]. The crosslinking of the fabricated device from the bare surface until the nanomaterial conjugation was performed via the selected chemical reactions. The chosen linkers promote a good binding due to its natural elemental compositions. This work has utilized a simple drop-cast method of MoS_2/Au-NPs onto BG-FET biosensor with an excellent LOD and sensitivity performance using current-voltage measurement. Furthermore, the mechanism of accumulation of electron/holes on BG-FET surface was illustrated to demonstrate the conduction layer formation, thus allowing the current to flow from the drain to the source region. The conduction layer was integrated with MoS_2 nanosheets, and Au-NP material shows highly sensitive and selective detection with the acceptable reproducibility and lower limit detection, which can be employed as a new method for the early detection of C-RP. In addition, a comparative study between the absence and presence of MoS_2/Au-NPs via ELISA was carried out to evaluate the detection performance.

Material and methods

Materials and reagents

A series of chemical reagents were from Sigma-Aldrich (Malaysia, www.sigmaaldrich.com): phosphate buffer solution (PBS) (100 mM, pH 7.4), 3-aminopropyltriethoxysilane (APTES), 1,1-carbonyldiimidazole (CDI), 16-mercaptohexadecanoic acid (16-MDA), and gold nanoparticle (Au-NP; 30 nm). Full-length mouse C-reactive protein monoclonal antibody and C-reactive protein were purchased from Abcam (Cambridge, MA, USA, www.abcam.com). 1-Ethyl-3-(3-dimethylaminopropyl) carbodiimide (EDC), and *N*-hydroxysuccinimide (NHS) were purchased from GE Healthcare (Malaysia, www.ge.com). In total, 18 mg/L of MoS_2 at 100 ml solution was purchased from Graphene Supermarket (Ronkonkoma, NY, USA, www.graphene-supermarket.com). TMB one-solution substrate for horseradish

peroxidase (HRP) was obtained from Promega (Malaysia, www.promega.com) and 5X ELISA coating buffer was purchased from Biolegend (San Diego, USA, www.biolegend.com). ELISA plates were acquired from Santa Cruz Biotechnology (Dallas, TX, USA, www.scbt.com), while Tween-20 was procured R & M Chemicals (www.m.evergreensel.com.my).

Enzyme-linked immunosorbent assay

By applying the conventional enzyme-linked immunosorbent assay (ELISA) method, two experimental procedures were presented to investigate the detection limits between conditions with the absence as well as the presence of Au-NPs/MoS_2 conjugation to capture C-RP antigen.

Absence of Au-NPs/ MoS_2

Different concentrations of C-RP antigen were serially diluted (100 nM down to 1 pM) in coating buffer (CB, from 5X to 1X dilution) and discretely coated the prepared antigen onto 96-well ELISA plate before leaving it for one night (> 16 h) incubation at 4 °C. Then, 3% of bovine serum albumin (BSA) was incubated for 1 h to avoid non-specific binding. Prepared dilution (1:1000) of primary C-RP antibody in blocking buffer was immobilized on each well for 2 h. Next, the secondary antibody dilution with a ratio of 1: 1000 (readily commercialized with HRP conjugation) was further added and left for incubation within 1 h. Control well was included to distinguish true-positive results and potentially false-positive results. Washing operation was performed 3 times consecutively for 10 min between each step using Tween-20 solution washing buffer (Tris Base:NaCl:distilled water). Finally, horseradish peroxidase (HRP) was added onto each well to verify C-RP antigen and C-RP antibody interaction and output. All the processes were done at room temperature except for the initial overnight incubation. The optical reading (OD) and the absorbance against concentration were observed and determined using a spectrophotometer with adjustment of wavelength at 405 nm and photographed. Results were recorded 10 min after the TMB substrate was added.

Presence of Au-NPs/MoS_2

In this experiment, all the processes that occurred were similar to the previous experiment. However, the preparation for initial serial dilutions of C-RP antigen was different. Similarly, different concentrations of C-RP antigen were diluted in CB (C-RP, CB)-(A). Next, the pre-prepared C-RP antigens were diluted with the chemical linkers (MoS_2 nanosheets, Au-NPs, 16-MDA, EDC: NHS)-(B). The mixture of A + B was then coated onto each well. After all the steps were finished, the results were then measured using a spectrophotometer and photographed after 10 min upon addition of the substrate.

Device preparation and functionalization

Fabrication process of field-effect transistor device

A *p*-type silicon-on-insulator (SOI) wafer (thickness: 70 nm (top silicon (top-Si) layer); 145 nm (buried oxide (BOX) layer); and 1000 μm (Si substrate layer)) was used to fabricate the back-gated field-effect transistor (BG-FET) device sensor. The process was started by cleaning the SOI wafer using a piranha solution (hydrogen peroxide: sulphuric acid at a ratio of 1: 3 and rinsed thoroughly in running distilled water). In this process, the conventional photolithography technique was used to obtain the source and drain regions of FET on the top-Si layer. The pattern transfer procedure for them was done using UV light exposure inside a mask aligner; wavelength and exposure period were 365 nm and 10s, respectively. Prior to the light exposure, the SOI wafer was coated with positive photoresist and used spin-coater to develop resist thickness and followed by the development process of substrate using a developer solution. The formation of the drain and source on the top layer was obtained using inductively coupled plasma reactive ion etching (RIE) to etch 100 μm size of channel width. Similar process of photolithography steps was performed to expose the substrate back-gate on bottom Si layer, followed by immersing the device in a buffered oxide etch (BOE) solution to etch an oxide layer. Au and nickel (Ni) contact pads were deposited and patterned via photolithography process and followed by wet etching using aqua regia solution (nitric acid: hydrochloric acid at a ratio of 1:3) to provide the platforms, allowing the flow of voltage supplies at source, drain, and back-gate. These processes were similar to the previous report [29]. The drain, source, and substrate-gate electrode, as well as the channel of the BG-FET device, were obtained, as illustrated in Fig. 1a.

Sensing channel mediated by Au-NPs and MoS_2 nanosheets

For the surface modification of Au-NPs/MoS_2 decoration on a 100-μm-width channel, the process was started by immersing the sensor into 2% of APTES and incubated for 1 h to increase sensor surface separation with charge biomolecule layer as well as to create amine-functionalized substrate [30]. Next, the mixture of EDC and NHS (EDC/NHS) with a concentration of 400 nM and 100 nM, respectively, was dropped on an active channel for 20 min to introduce carboxyl functionalities group [31] and bind with amine group by aforementioned APTES deposition. The APTES/EDC:NHS surface was further functionalized with 16-MDA acid and incubated for 1 h to bind with carboxyl functionalities group in EDC:NHS crosslinking and also to create thiol-linkage in order to bind with Au-NPs later. This APTES/EDC:NHS/16-MDA was further modified by Au-

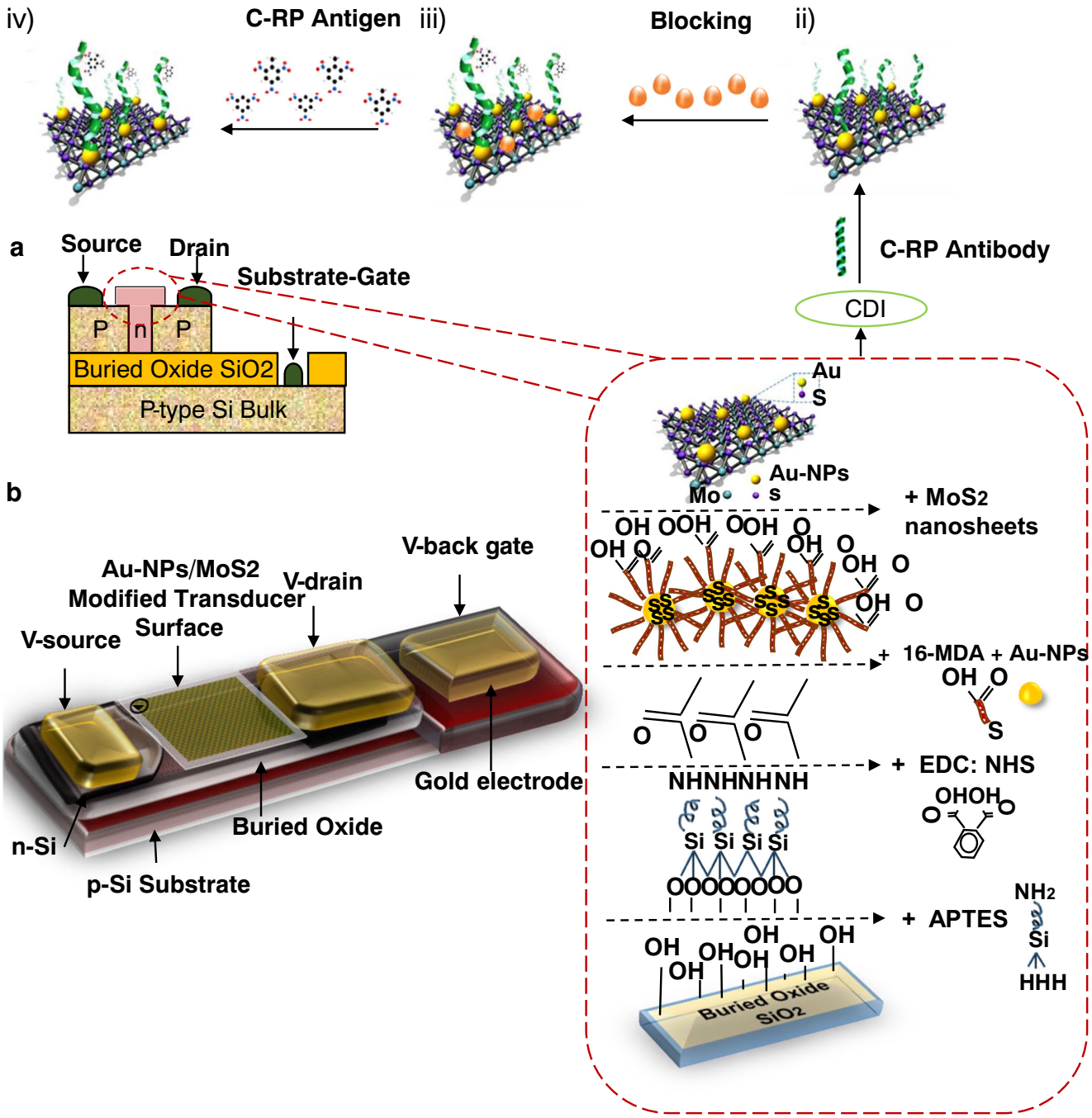

Fig. 1 (**a**) Schematic diagram of field-effect transistor device fabricated on SOI wafer. (i) Surface functionalization process with MoS_2 and Au-NPs deposition. (ii) Immobilization process of C-RP antibody on Au-NPs/MoS_2 modified surface. (iii) Blocking process with ethanolamine. (iv) Detection of C-RP antigen on channel between source and drain. (**b**) Complete illustration of Au-NPs/MoS_2-based BG-FET

NPs and MoS_2 nanosheet solutions. In order to mediate high and excellent performance of C-RP antigen detection, Au-NP solution with a volume of 3 μL was incubated for 1 h and followed by 3 μL of MoS_2 nanosheet solution and also left for 1-h incubation. The incubation hours for Au-NPS and MoS_2 nanosheets were optimized to allow a good binding amount of sulphur group in MoS_2 nanosheets in order to trap the atoms in Au-NPs effectively, thus creating a great chemical bonding between them [32].

All the incubation processes for surface functionalization were done at RT. The full linking process of APTES/EDC:NHS/16-MDA/Au-NPs/MoS_2 deposition is illustrated in (Fig. 1a (i)).

Immobilization and detection of C-RP on surface

The device prepared with Au-NPs/MoS_2 deposition was then continued for the immobilization process. After the previous

surface functionalization process, 5 mM of CDI was continued for functionalization on a channel and left for 1-h incubation to assist in the binding with C-RP antibody. After that, 1 μm of C-RP antibody was constantly immobilized on a channel at room temperature for 1 h then washed with PBS with a concentration of 10 mM (Fig. 1b (ii)). After immobilization, the surface was treated with 1 M of ethanolamine and incubated for 20 min to avoid the non-specific biofouling on Au-NPs/MoS_2-functionalized surface (Fig. 1 b (iii)). For the detection event, various C-RP antigen concentrations (10 ng/mL, 1 ng/mL, 100 pg/mL, 10 pg/mL, 1 pg/mL, and 100 fg/mL) were diluted in 100 mM PBS and incubated for 10 min at each concentration (Fig. 1b (iv)). This incubation was performed to allow C-RP antigen to bind with the immobilized C-RP antibody on the surface. The processes/steps of measuring the device's performance before and after surface modification, immobilizing, and target detection were done via the electrical measurement using a semiconductor parametric analyser (SPA) (Keithley 6487 SPA; Keithley Instruments, Cleveland, OH, USA).

Reproducibility, selectivity, and demonstration of C-RP in human serum analyses

Three numbers of BG-FET sensors ($n = 3$) were tested for reproducibility analysis. The measurement was repeated three times on different devices. The modified surface sensors were measured with five different concentrations ranging from 100 fg/mL to 10 ng/mL. For the selectivity test, five numbers of samples were tested for this experiment. For the first part of the selectivity test, a non-specific binding measurement was carried out by releasing 1 μg/mL of cardiac troponin I (cTn1) protein and 1 μg/mL of bovine serum albumin (BSA), independently, onto 10 μg/mL C-RP immobilized surfaces for distinction purposes. For the second part of the selectivity test, 1:1000 dilution of human blood serum was dropped onto the Au-NPs/MoS_2-modified channel loaded with an antibody-immobilized surface. For the third part of the selectivity test, 1 pg/mL of C-R antigen and followed by 1 ng/mL of C-R antigen was spiked with 1:1000 human serum dilution and directly drop onto the immobilized transducing channel.

Results and discussion

Verification on detection limit via conventional ELISA

Figure 2a shows a visual observation of a conventional ELISA plate with the modification of Au-NPs and MoS_2 nanosheets for C-RP antigen (100 nM down to 1 pM) binding with C-RP antibody. Initially, the comparisons in terms of determining the detection limit were made in the absence (Fig. 2b) and presence (Fig. 2c) of Au-NPs and MoS_2 nanosheets. As a result, the significant colour shifted once adding the substrate onto each well. As expected, the specific well with uncoated C-RP (control) has displayed no colour changes. The colour change was noticed to appear at 100 nM (equivalent to 11.5 μg/mL) for Au-NPs/MoS_2 absence, while 100 pM (equivalent to 11.5 ng/mL) for Au-NPs/MoS_2 presence. This result demonstrated the detection limit is within the range of 10 pM to 100 nM (absence) and 10 pM to 100 pM (presence). For the absence of Au-NPs/MoS_2, the change in colour becomes obvious and turns from clear to dark blue solution as the concentration increases. Different from the presence of Au-NPs/MoS_2 nanocomposite conjugation, the colour was initially clear and turned to light blue before returning to its clear state (red circle). This can be attributed to the increasing concentrations of C-RP, more enzyme-linked antibody/Au-NPs/MoS_2 has possibility to attach onto the edges of the wells, thus lowering the unbound antibody label [33]. As a result, it shows a good detection limit of C-RP antigen in the presence of Au-NPs/MoS_2 compared with the absence of Au-NPS/MoS_2 nanosheets. The peak obtained has proved that the conjugation between these two nanomaterials has improved the catalytic activity, thus enhancing the biomolecules captured into the enhanced ELISA plates. Table 1 shows the optical density reading for various C-RP target concentrations with and without the presence of Au-NPs/MoS_2 nanosheet conjugation. Significant increases were spotted in optical density with 0.72 (at 100 nM) and 0.43 (at 100 pM) for the presence and absence of Au-NPs/MoS_2, respectively. Higher quantity of C-RP target resulted in higher number of binding in the wells with C-RP antibody. Next, the performance was further investigated using a label-free back-gated FET biosensor in the later section.

UV-visible spectrophotometry

UV-Vis absorption spectrum is a well-known approach which declared the nature prescription of selected materials, such as MoS_2 nanosheets. Therefore, MoS_2 nanosheet solution at a concentration of 18 $mg{\cdot}L^{-1}$ was analysed; thus, these obtained peaks represent the properties of 2D MoS_2 nanosheet material [34] as shown in Fig. 3a. In particular, an indirect bandgap for MoS_2 bulk crystal was presented from ~ 1.2 to 1.3 eV, while a direct bandgap for mono-layered MoS_2 was opened from ~ 1.7 to 1.9 eV. Therefore, these regions certainly displayed two sharp peaks centred at A ~ 660 nm (1.83 eV) and B ~ 611 nm (1.99 eV), proving that they are mono-layered structures. These two peaks also represented an exciton splitting phenomenon and revealed a separation with ~ 49 nm [34, 35]. Then, broader peak C was verified and positioned at ~ 450 nm (2.73 eV). Peak C can be described as the electron to move in the direct transition from one band to another band [34]. These results meet an agreement with the previous findings [35, 36].

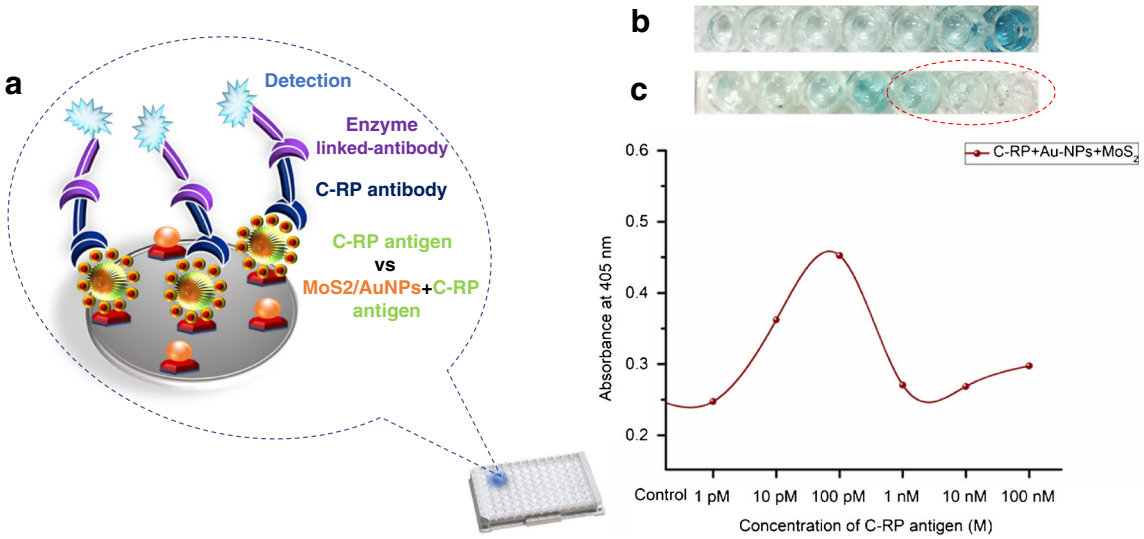

Fig. 2 **a** Visual inspection on the microtiter plate for limit detection verification of C-RP target by conventional ELISA. **b** Absence of Au-NPs/MoS_2 nanosheets. **c** Presence of Au-NPs/MoS_2 nanosheets

Raman spectroscopy analysis

Raman spectral analysis is one of the non-destructive techniques to investigate the crystallinity and transport properties of material. Generally, the Raman measurement enables to exhibit typical bands for MoS_2, which are E^1_{2g} (out-of-plane), longitudinal mode, and A_{1g} (in-plane) transversal mode [8, 37]. The former E^1_{2g} can be attributed to the vibrations of two S atoms with Mo atom, while A_{1g} corresponded to the vibrations of S atoms in opposite directions. Figure 3b shows a Raman spectrum of MoS_2 nanosheets and after the introduction of Au-NPs to the MoS_2 nanosheets. From the observation, the Raman spectrum of MoS_2 nanosheets (blue curve) exhibits two peaks at 382.34 cm^{-1} (E^1_{2g}) and 405.62 cm^{-1} (A_{1g}); the ranges are in agreement with those of previous report [17, 38, 39]. After the introduction of Au-NPs to the MoS_2 nanosheets (orange curve), the Raman intensity and frequency of MoS_2 molecules are slightly enhanced. The peaks were broadening and this indicated a better enhancement effect of Au-NPs [38, 39]. In addition, two band intensities in MoS_2/Au-NP nanohybrids were enhanced approximately by ~30%. These significant changes show the existence of chemical bonding between MoS_2 nanosheets and Au-NPs, proving hot plasmonic electron of Au nanoparticles gives the effect to the photoluminescence and absorption behaviour on MoS_2 nanomaterial [9].

Table 1 Optical density for various concentrations of C-RP antigen binding with C-RP antibody only and C-RP antibody with Au-NPs/MoS_2 nanosheet conjugation

Concentration	Optical density (O.D.)	
	C-RP	MoS_2-Au-NPs/C-RP
Control	0.379	0.254
1 pM	0.419	0.247
10 pM	0.555	0.362
100 pM	0.334	0.453
1 nM	0.437	0.270
10 nM	0.326	0.269
100 nM	0.716	0.298

Visual inspection and surface morphology characterization

Visual inspection and morphological characterization of MoS_2 nanosheet solutions and Au-NPS were carried out using HPM and SEM. Figure 4 a and b show Au-NP material and Au-NP-structured MoS_2 nanosheets, respectively, by the visual inspection via HPM to observe the uniformity of the surface before and after drop-cast MoS_2 nanosheet solution. The Au-NPs were clearly visible in Fig. 4a. Figure 4b shows the uniform structured layer of Au-NP material and MoS_2 nanosheets conjugation on the surface at × 100 magnification. Nevertheless, few areas were spotted to be uneven and restacked. Figure 4c and d show the surface morphology of Au-NP nanoparticles and Au-NP-decorated MoS_2 nanosheets, respectively, by SEM. In Fig. 4c, the Au-NPs could clearly be observed on the SiO_2 surface. However, the aggregation of Au-NP nanomaterials was clearly visible, forming a large area of aggregation (Fig. 4c). The unavoidable aggregation might occur due to unknown reasons, for example, the large surface energy and wide specific surface area of Au-NPs; hence, it is thought to control the architecture of Au-NP nanostructure [18]. Figure 4d shows that Au-NPs selectively prefer MoS_2 nanosheets and show that Au-NPs were

well-dispersed on the MoS_2 nanosheets. The incorporation of these nanomaterials seems achievable since they could be attached together. However, uneven surface of Au-NPs/MoS2 conjugation layer can be seen through the image. Theoretically, the stacking phenomenon may occur due to the smaller sheets which may contain smaller van der Waals attraction as well as weaker hydrophobic force [40]. This condition may reduce by applying less repulsive force and conduct appropriate ultrasonication processes to prevent them from restacking [41]. Figure 4e shows the area of Au-NPs/MoS_2 nanosheet deposition on the transducing channel, and Fig. 4f shows an approximately 100 μm size of width channel.

Surface morphology of MoS_2 nanosheets, Au-NPs, and MoS_2/Au-NP modification on SiO_2 substrate was presented in Fig. 5 by using AFM. MoS_2 nanosheets were drop-casted on SiO_2 layer to validate the dimension and thickness sizes before conjugating with Au-NPs as shown in Fig. 5a (i) to (ii). The lateral dimension and also the thickness of MoS_2 nanosheets approximately range from 100 to 300 nm and 15 to 35 nm, respectively, as shown in Fig. 5a (iii). Similar obtained results of MoS_2 thickness also have been reported by [30] through the exfoliation treatment. Next, Fig. 5b (i) to iii) show the surface morphology of Au-NP deposition followed by the conjugation of MoS_2 nanosheets and Au-NPs on SiO_2 substrate (Fig. 5c (i) to (iii)). The conjugation of Au-NPs and MoS_2 nanosheets was further characterized to observe the uniformity of the surface. Initially, the surface was pretreated with APTES, EDC: NHS, and 16-MDA before the deposition of Au-NPs and MoS_2 nanosheets to allow a strong linking of Au-NPs and MoS_2 on the SiO_2 surface. As a result, the nanocomposition of MoS_2 nanosheets and the Au-NPs was well dispersed on the surface. However, the thickness and dimension of Au-NPs obtained were quite large compared with the original dimension used (30 nm) (Fig. 5a (iii)). This event was suspected to occur due to the aggregation of nanoparticles and the dimension ranged from 70 to 200 nm. Despite this aggregation event, the conjugation seems to work due to the surface affinity effect between MoS_2 and Au-NPs, which made the Au-NP to selectively capture and prefer MoS_2 nanosheets layer [13]. In this research, gold was selected to showcase electronic configuration of catalytically active gold as reported in [42].

Voltammetry analysis on the interaction of C-RP antigen/antibody via Au-NPs/MoS_2 back-gated FET

The detection of C-RP antigen by its particular antibody was carried out as shown in Fig. 6. The performance of Au-NPs/MoS_2 biosensor was further conducted by measuring the current-voltage detection of the modified channel, antibody immobilization, detection responses at different antigen concentrations, LOD, and sensitivity performances. Prior to the charge variation of molecules, each layer of surface modification showed the current changes and increased subsequently as shown in Fig. 6a. Starting from the surface modification with APTES, it has been utilized to introduce the amine-terminated group, thus activating the SiO_2 layer to ease the binding of biomolecules [43]. After the deposition of APTES, the current increased until 25 nA between the channel while biasing the back gate at Vgs = 1 V (Vds = 2.0 V), showing a good interaction upon attaching amine-terminated group with SiO_2. Next, the Au-NPs and MoS_2 nanosheets were deposited and the current increased until 158 nA due to high electron transfer and high conductivity [44] of Au-NPs (neutral charge attracts a layer of ions of opposite charge to the nanoparticle surface) and MoS_2 (n-type material, high electron charge) between source and drain. This phenomenon can be explained when the accumulation of a high hole concentration occurs in *p*-type Si substrate (biasing Vgs = 1 V); these charges were creating the inversion space charge circumstances in the *p*-type substrate along the BOX/*p*-type Si substrate interface, cross-sectional line (Fig. 6c). When the electric field was induced, it penetrates the semiconductor; the holes in the *p*-type silicon substrate have experienced a force towards the oxide

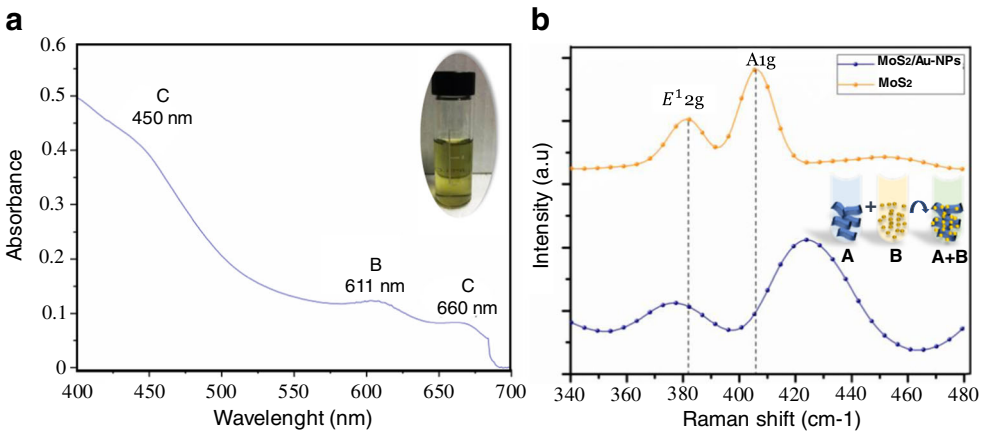

Fig. 3 **a** UV-Vis analysis exhibits peaks A, B, and C to prescribe the MoS_2 nanosheet properties. **b** A comparative Raman spectrum shifting for MoS_2 nanosheets and Au-NPs/MoS_2 nanosheets. **b** Shows hybridization process where A and B indicate MoS_2 nanosheets and Au-NPs, respectively

(SiO_2/BOX interface, cross-sectional line [Fig. 6d]) and attracted the electron charge between the source and drain channel, thus creating an accumulation of electron along the interface and producing an electron conduction layer at the channel [29]. Advantageously, the decorated materials lead to light control activation from MoS_2 excitation energy band and promote the high affinity of the FET device [44]. The incorporation between these two materials enhanced the electron conduction layer and this is the turning point of the current to be significantly increased after the deposition of MoS_2 nanosheets. The multi-layer-modified surface in active area (channel) had revealed the current was gradually increased from pristine until the drop-cast of MoS_2 nanosheet solution measurements. Besides, the C-RP molecules were successfully immobilized onto the modified device, thus showing higher current response. The immobilization indicates that a successful binding event occurs between the device surface and C-RP antibody. The surface modification by Au-NPs/MoS_2 provides abundance of active sites on the nanosheets for loading higher C-RP antibodies, thus allowing more C-RP antigen to

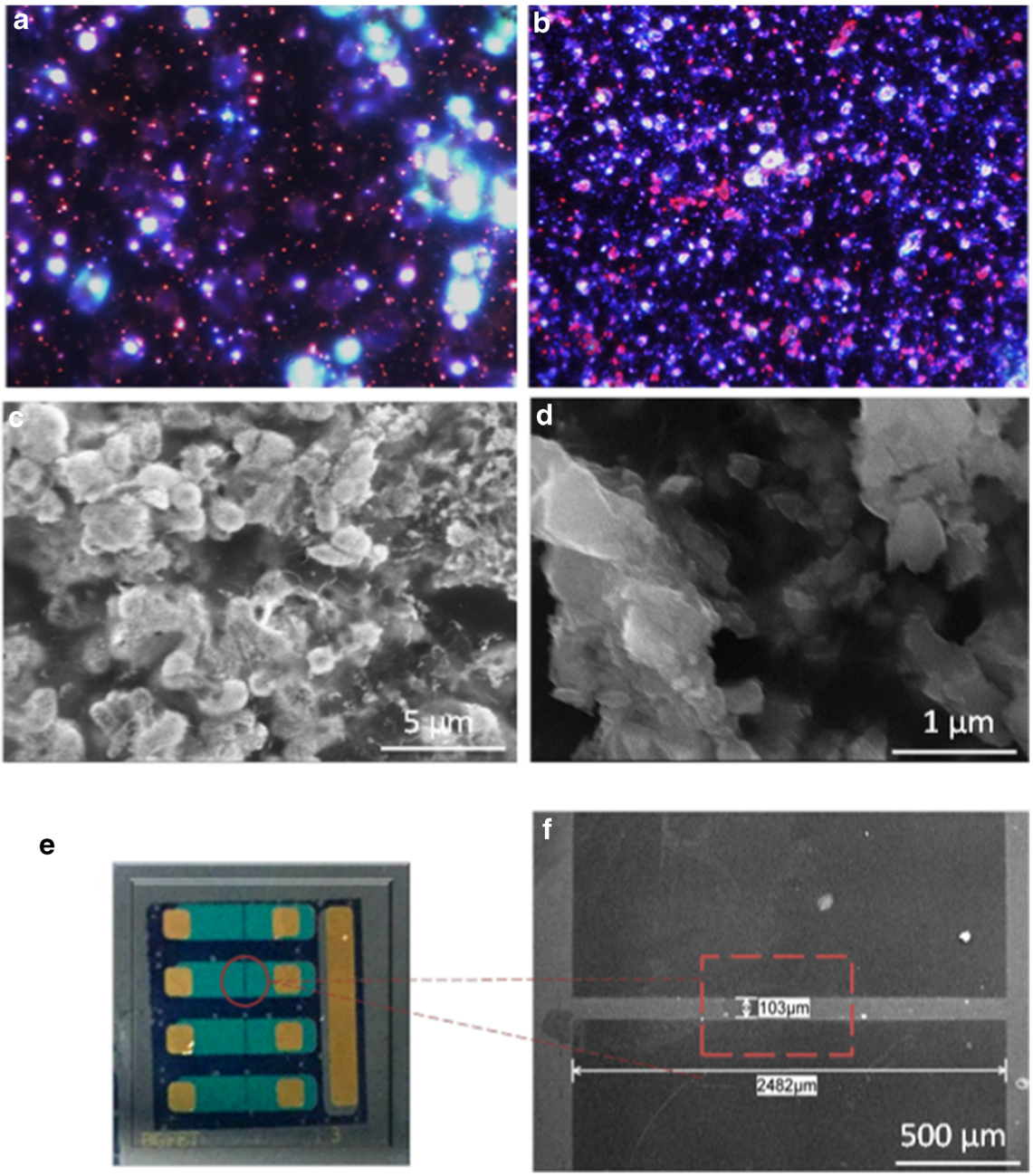

Fig. 4 Surface morphological images of Au-NP material (**a**) and Au-NP-structured MoS_2 nanosheets (**b**) at × 100 magnification using HPM; MoS_2 nanosheets (**c**) and Au-NP-structured MoS_2 nanosheets (**d**) at × 1000 magnification using SEM. **e** Photograph of back-gated FET with transducing channel; **f** active channel area. About 100 µm width as shown by SEM, where all the modifications occur

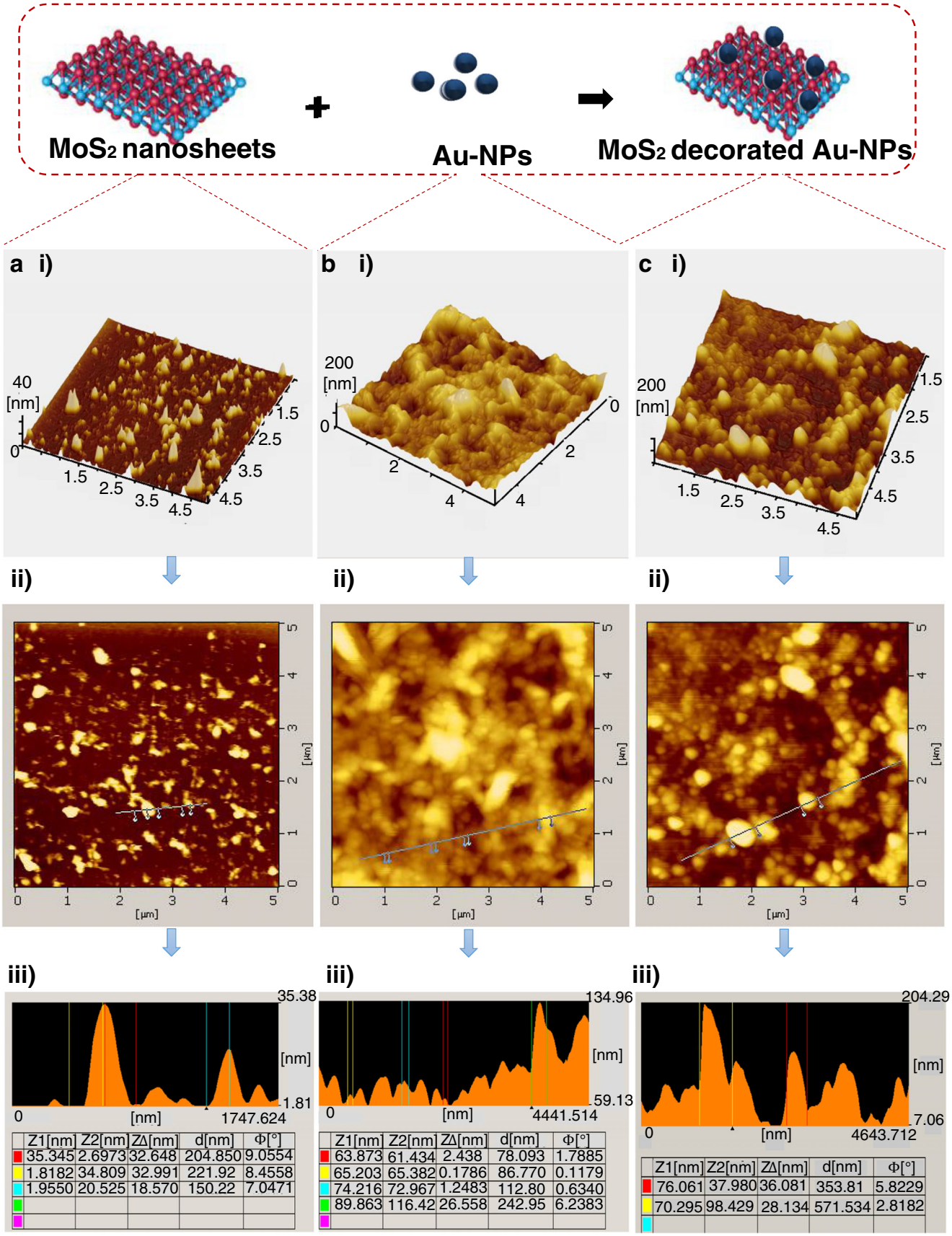

Fig. 5 AFM images of (a) (i) to (iii) MoS_2 nanosheets (b) (i) to (iii) Au-NPs material (c) (i) to(iii) Au-NPs structured MoS_2 with the size dimension and thickness for each deposition.

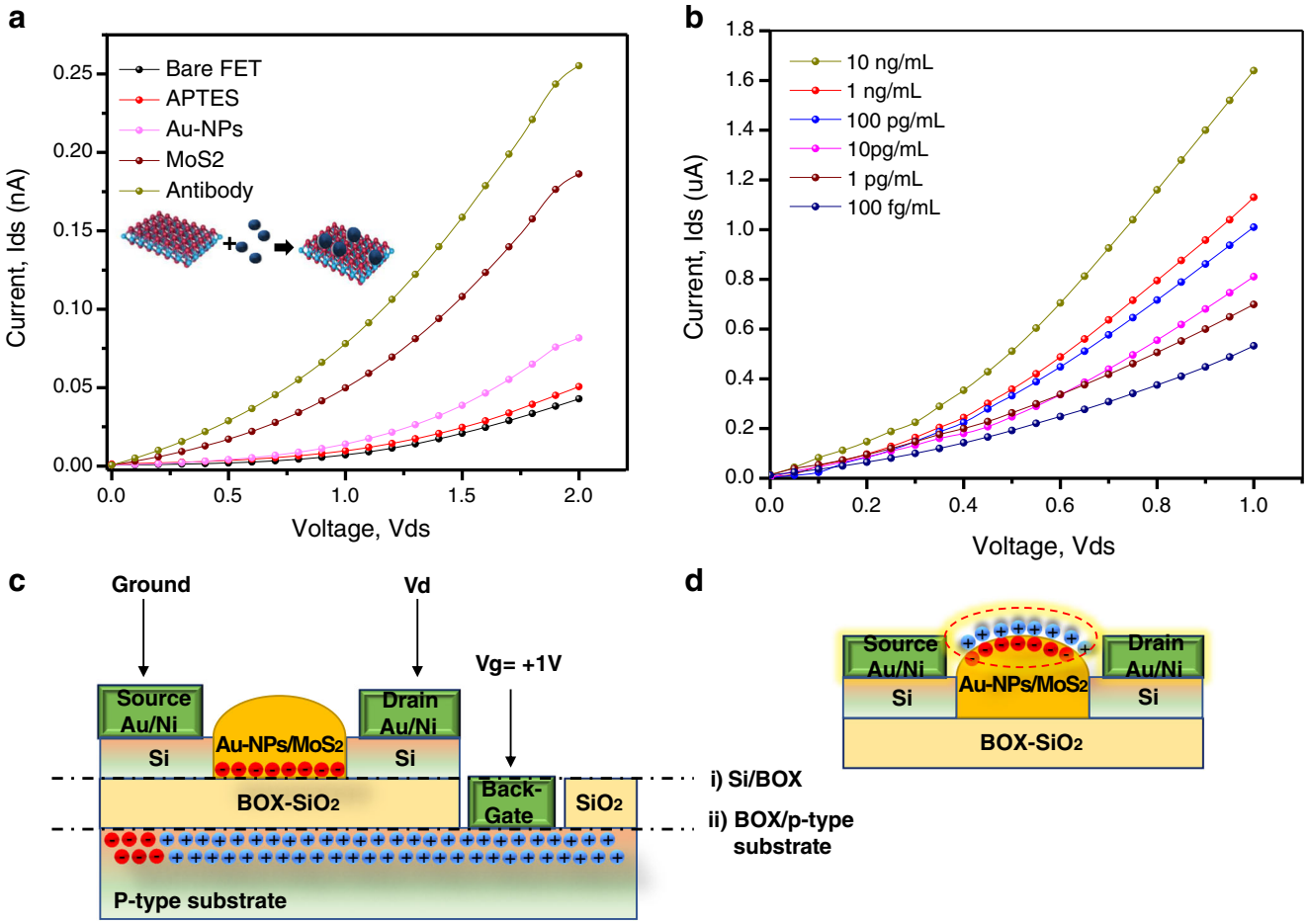

Fig. 6 Ids against Vds characteristic for BG-FET biosensor (Vbg at 1 V) (**a**) surface modification with Au-NPs and MoS_2 nanosheets until immobilization step (**b**) detection at different C-RP antigen concentrations on Au-NPs/MoS_2-BG-FET biosensor between the range of 100 fg/mL and 10 ng/mL. Illustration of the effect of carriers towards (**c**) hole concentration at BOX/p-type Si substrate interface and electron concentration at SiO_2/BOX interface (**d**) electron charges inside the transducing channel and positive charges of C-RP biomolecules at detection surface (red circle)

be interacted, which amplifies the signal of electrochemical effect.

The electrical result of current-voltage (I–V) after C-RP antibody-antigen binding event was shown in Fig. 6b. The device exhibits a significant increment as the biomarker concentrations were increased from 100 fg/mL to 10 ng/mL. This is because of positively charged target C-RP (C-RP isoelectric point (pI) = 9.2 [45], thus carrying more positive charges), while biasing the substrate-gate electrode (Vgs = +1 V) has attracted electron carrier inside the Au-NPs/ MoS_2 channel region due to the opposite charges and increased the electron concentration. Further enhancement of the electron conduction layer between the *p*-type source and drain allows more current to flow (dotted circle in Fig. 6 (e) (iii)). These explain the increased value of Ids while increasing the concentrations of C-RP antigen. Higher concentration results in higher density of biomolecules. Furthermore, the binding event of MoS_2 and charged biomolecules at interface allows a great current conduction due to its efficient incorporation and stability in liquid form [30, 46]. This phenomenon can be elucidated that a unique 2D structure of MoS_2 has contributed to the enhancement and high sensitive detection of C-RP [44]. Also, surrounding net charges of FET biosensor enable the influence of carrier movement transport in MoS_2 material between the source and drain [44].

Limit of detection and sensitivity studies on the developed BG-FET sensor: High performance

In this research, the linear calibration curve (ΔIds against Vds) was computed to determine the limit of detection (LOD) and the sensitivity level of the developed biosensor. The performance of developed Au-NPs/MoS_2-BG-FET biosensor for the quantitative analysis of C-RP antigen was investigated. The LOD is defined as the smallest concentration of an analyte in the test sample that can be reliably quantified by an analytical process [28]. The calibration curve in Fig. 7a shows the capability of the sensor for a linear detection of C-RP antigen in the range of 10 ng/mL down to 100 pg/mL, following the equation ΔIds (μA) = 0.176 log (C-RP concentration in

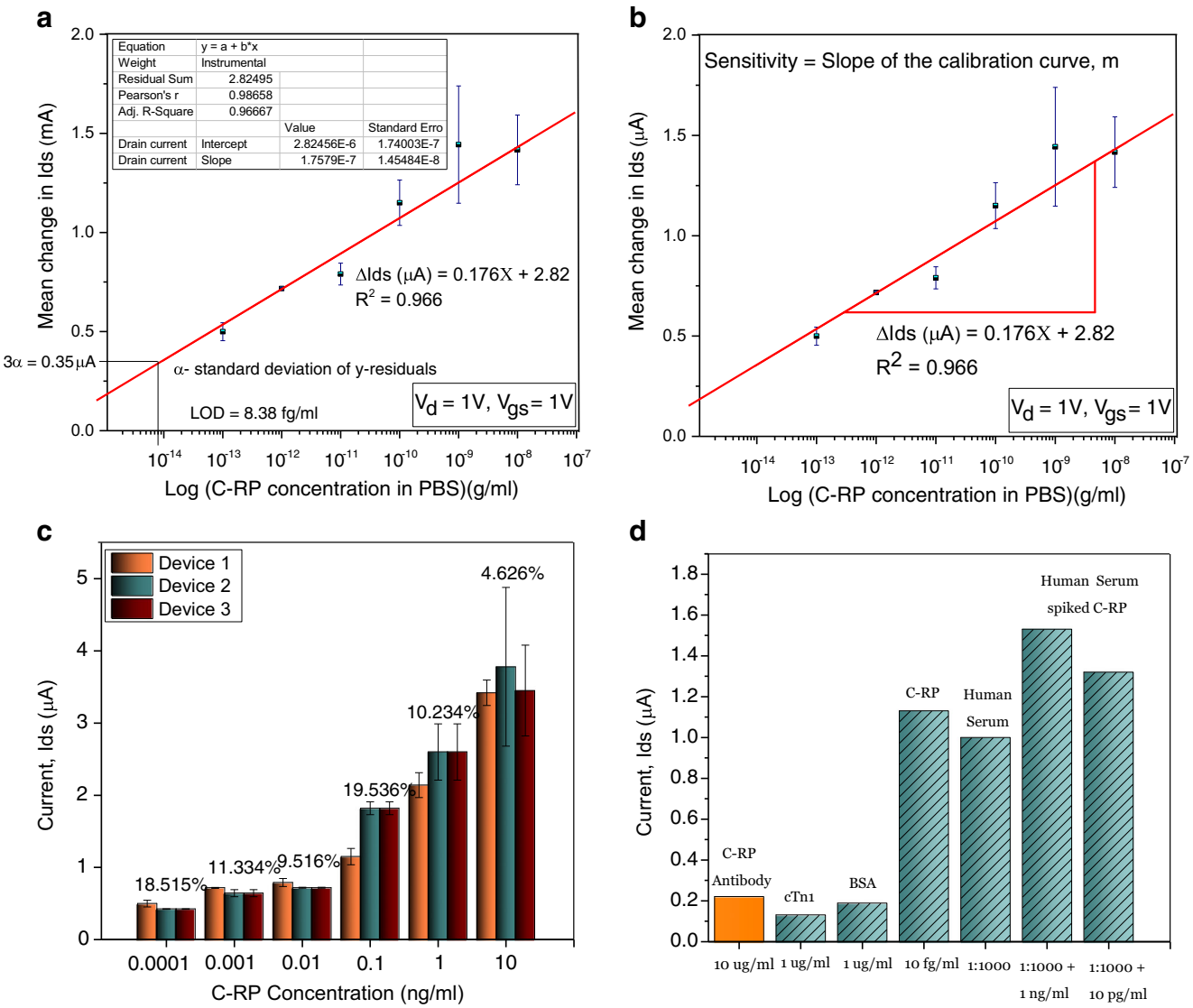

Fig. 7 Change of Ids against Vds in calibration curve (**a**) for LOD detection; **b** quantitative analysis on sensitivity performance of device; **c** reproducibility ($n = 3$) with calculated RSD; **d** selectivity of C-RP antibody against different proteins ($n = 5$) at Vd = 1 V, Vgs = 1 V

PBSA) (g/mL) + 2.82 [μA]. The sensors exhibit a sensitivity of 0.176 log (C-RP concentration in PBS (g/mL) with a correlation coefficient (R^2) of 0.966. The LOD was estimated as 8.38 fg/ml, using the linear regression analyses [47]. The LOD estimation was expressed using the formulae:

$$LOD = \frac{3\alpha}{b}$$

where α is the standard deviation of the biosensor's response, where it was estimated from *y*-residuals of the calibration curve and *b* is the sensitivity of the biosensor determined from the slope of the calibration curve. The closer the R^2 is to 1, the more precise the measurement and will result in a more relevant assessment [48]. Table 2 shows the comparison of the immunosensors of the reported works with other assays. The previous researches demonstrated the uses of MoS_2 nanomaterial-conjugated noble material Au-NPs to obtain a linear and acceptable detection limit for various types of targets inclusive of C-RP antigen. It was noticed that the developed sensor exhibits a comparable linear detection range with other reported assays. The developed biosensor in this work presented a low limit of detection and good sensitivity output which can be ascribed to these by the following justifications. Firstly, the introduction of back-gate biasing allows more current to easily flow through Au-NPs/MoS2-modified sensing channel, thus accelerating the charges inside the nanomaterials to attach the biomolecule. Secondly, this developed label-free biosensor also found to be simpler since this study was not dealing with the additional nanomaterial, such as graphene to enhance the surface capability. This is due to the functional linker used which has contributed to a great binding. For example, 16-MDA is crosslinking to create a

Table 2 Performance comparison of the developed biosensor for c-reactive protein detection

Scheme	Fabrication hierarchy	Detection range	LOD	Unit	Assay	Reference
Au-NPs/MoS2-GCE	GCE/Au-NPs/MoS2/Ab_1/ Ab_2/BSA/insulin	0.1p - 1n	50f	mol/L	CV/EIS	[14]
Au-NPs/MoS2-Gas/GCE	GCE/Au-NPs/MoS2-GAs/anti-PSA/BSA/PSA	0.00001 n – 50 n	0.003 p	g/mL	DPV/EIS	[22]
Au-NPs/3D MoS2-rGO/GCE	GCE/Au-NPs/MoS2-rGO/GCE -hydroquinone -catechol -resorcinol	0.1 μ - 950 μ 3 μ - 560 μ 40 μ 960 μ	0.04 μ 0.95 μ 14.6 μ	M	DPV	[23]
Au-NCs@MoS2/Au@PtNPs/gold electrode	Gold electrode/ Au-NCs@MoS2/Au@PtNPs/anti-MC-LR/BSA/MC-LR	1.0 n – 1.0 m	0.3 n	g/L	CV/DPV/EIS	[49]
P-channel ISFET	Si/SiO_2-CeO2/streptavidin-biotin/anti-C-RP	100 n – 250 n	100 n	g/mL	I-V	[50]
AuNW/PC substrate	Au substrate/ MPA/EDC:NHS/anti-C-RP/BSA	5 f – 220 f	2.25 f	g/mL	CV/EIS	[5]
Pt-RTD	Pt-RTD/SiO_2/Au/Cy3-conjugated protein G/anti-C-RP/BSA/C-RP/Au-NPs-conjugated polyclonal anti-C-RP	0.1 n – 100 n	0.1 n	g/mL	Visual/thermal analysis	[51]
Bio-HEMT/Ref-HEMT/QRE	HEMTs/AlGaN/GaN/PCB/MUA/ EDC:NHS/anti-C-RP	0.01 n - 100 n	0.01 n	g/mL	I-V	[3]
Au-SPE	Au-SPE/MES/EDC:NHS/anti-C-RP	70 p – 1 μ	0.021 n ± 5 p	g/mL	Ampero	[52]
Gold electrode	Gold electrode/EDC:NHS/anti-C-RP	57.5 n – 5.75 μ	20.24 n	g/mL	EIS	[4]
MoS_2/Au-NPs-based back-gated FET	Si/SiO_2/APTES/EDC:NHS/16-MDA/Au-NPs/MoS_2	100 f – 10 n	8.38 f	g/mL	I-V	This work

ISFET, ion-sensitive field-effect transistor; *MPA*, 3-mercaptopropionic acid; *Pt-RTED*, platinum-resistive temperature detector; *HEMT*, high electron mobility transistor; *QRE*, quasi-reference electrode; *FET*, field-effect transistor; *MoS2*, molybdenum disulfide; *Au-NPs*, gold nanoparticles; *Au-NCs*, gold nanoclusters; *rGO*, reduced grapheme oxide; *PtNPs*, platinum nanoparticles; *MC-LR*, microcystin-LR

thiol-linkage event with Au-NPs, thus enabling the loading of Au-NPs on the surface. Interestingly, the results showed that this BG-FET biosensor was capable of biosensing cardiovascular disease at 8.38 fg/mL of C-RP antigen concentration. Apart from that, the MoS_2/Au-NPs-BG-FET has attained a better (LOD) compared with the conventional MoS_2/Au-NPs-ELISA, which is 11.5 ng/mL. The MoS_2/Au-NPs-BG-FET has proven to be a feasible potential candidate for low-cost and rapid biosensing applications.

Reproducibility and selectivity analyses of developed sensor

A reproducibility test was conducted to evaluate the repeatability and precision of the developed sensor using (I–V) measurement. Figure 7c shows the data of bar graph together with SD errors of a batch of three ($n = 3$) tested sensors, together with relative standard deviation (RSD) of diluted C-RP concentrations ranging from 100 fg/ml to 10 ng/ml. The result demonstrated an acceptable reproducibility with the highest RSD of 19.536% ($n = 3$). The high RSD might be attributed to the aggregation or assemble of MoS_2 nanosheets on the modified surface, which causes uneven surface on the device, however, producing a minor variation with the error analysis. Next, a selectivity test was conducted by monitoring the performance of device in the presence of different abundant proteins in human serum, interacting with C-RP antibody-immobilized Au-NPs/MoS2 surface (Fig. 7d). In this study, 1 μg/mL of cardiac troponin I (cTn1) and 1 μg/mL bovine serum albumin (BSA) were used to analyse the selectivity performance against C-RP antibody on the modified surface. The cTnI protein was interacted on the antibody-immobilized surface and also by BSA. These two samples were measured with their interactions and recorded. As a result, there were no significant differences in the current flow with cTnI (0.13 μA) and BSA (0.18 μA), from C-RP antibody immobilized on Au-NP/MoS_2 surface (0.22 μA). Even though the modified Au-NPs/MoS2 nanosheets can provide plenty of binding sites for proteins and also to elevate the current flow response due to its large surface area [14], the specificity test still shows no clear changes in the current with these uninteractive proteins. On the other hand, the current analytical test revealed a clear detection upon C-RP antibody-antigen interaction compared with other existing proteins in the human serum and gave a current reading of ~ 1.13 μA.

We also evaluated the occurrence of C-RP in diluted human serum alone on the antibody-immobilized biosensor. As a result, 1:1000 dilution of standalone human serum shows a current reading of ~ 1.02 μA after passing on the antibody-immobilized surface. The current flow was increased from C-RP antibody due to the originally existing C-RP protein in human serum. Nevertheless, the current level change from human serum alone demonstrates a reduction as in the aforementioned independent C-RP antigen. To further validate the selectivity performance of Au-NPs/MoS_2-modified sensor, the experiment was conducted by spiking the diluted human serum with 1 ng/mL and 10 pg/mL of C-RP concentrations. At these two concentrations, the device shows excellent selectivity signals from C-RP-spiked human serum recorded as 1.53 μA (1 ng/mL) and 1.32 μA (10 pg/mL). This significant increment might occur due to the abundance of C-RP protein in human serum. In addition, these results are also elucidated by the absence of interference by other major proteins such as albumin and globulin and small molecules from the serum. Despite these notable results, there were a few challenges encountered while completing this work. Firstly, multiple steps of chemical reactions and the optimization of deposition volume are quite challenging when dealing with the nanometre-sized channel. The channel needs to be precisely covered to avoid the dispersement of nanomaterials to the contact pad. Besides, the responsibility to monitor the 100-μm-sized channel during the fabrication process is quite tedious in order to prevent the over-etching. Considering the storage lifetime and the operational lifetime of the bare, sensing surface can be prolonged for several months under a proper storage condition with desiccator. However, upon immobilizing the biomolecule, the surface activity was found to be lost ~ 25% after 3 weeks and a further sharp reduction in a few days.

Conclusion

In summary, a label-free approach of FET device with back-gated biasing for the detection of C-RP antigen in the presence of Au-NPs/MoS_2 as transducing materials has been successfully described. The modification by Au-NPs/MoS_2 materials has proved the enhancement of device performance and can be considered a potential candidate in future heart disease diagnosis approaches. It further emerges the suitability to be integrated with CMOS technology for future hand-held devices. However, there are some limitations of this assay for C-RP detection as discussed above. Also, the operation is found to be unreliable in complex environment because external interference might affect biosensing performance.

In the future, the analyses will be extended to more available electrochemical measurement methods in order to investigate the biosensor performance precisely. The proposed nanomaterials will also be incorporated with other potential polymers to promote high sensitive detection.

Funding The author would like to acknowledge the support from the Fundamental Research Grant Scheme (FRGS) under a Grant no. of FRGS/1/2017/STG05/UNIMAP/03/3 from the Ministry of Education Malaysia.

Compliance with ethical standards

Conflict of interest The author(s) declare that they have no competing interests.

References

1. Black S, Kushner I, Samols D (2004) C-reactive protein. J Biol Chem 279:48487–48490. https://doi.org/10.1074/jbc.R400025200
2. Kokkinos C, Prodromidis M, Economou A, Petrou P, Kakabakos S (2015) Disposable integrated bismuth citrate-modified screen-printed immunosensor for ultrasensitive quantum dot-based electrochemical assay of C-reactive protein in human serum. Anal Chim Acta 886:29–36. https://doi.org/10.1016/j.aca.2015.05.035
3. Lee HH, Bae M, Jo SH, Shin JK, Son DH, Won CH, Lee JH (2016) Differential-mode HEMT-based biosensor for real-time and label-free detection of C-reactive protein. Sensors Actuators B Chem 234:316–323. https://doi.org/10.1016/j.snb.2016.04.117
4. Bryan T, Luo X, Bueno PR, Davis JJ (2013) An optimised electrochemical biosensor for the label-free detection of C-reactive protein in blood. Biosens Bioelectron 39:94–98. https://doi.org/10.1016/j.bios.2012.06.051
5. Vilian ATE, Kim W, Park B, Oh SY, Kim TY, Huh YS, Hwangbo CK, Han YK (2019) Efficient electron-mediated electrochemical biosensor of gold wire for the rapid detection of C-reactive protein: a predictive strategy for heart failure. Biosens Bioelectron 142: 111549. https://doi.org/10.1016/j.bios.2019.111549
6. Kutova O, Dusheiko M, Klyui NI, Skryshevsky VA (2019) C-reactive protein detection based on ISFET structure with gate dielectric SiO2-CeO2. Microelectron Eng 215:110993. https://doi.org/10.1016/j.mee.2019.110993
7. Song X, Xu J, Liu L, Lai PT, Tang WM (2019) Improved interfacial and electrical properties of few-layered MoS 2 FETs with plasma-treated Al 2 O 3 as gate dielectric. Appl Surf Sci 481:1028–1034. https://doi.org/10.1016/j.apsusc.2019.03.139
8. Krishnamoorthy K, Pazhamalai P, Veerasubramani GK, Kim SJ (2016) Mechanically delaminated few layered MoS2 nanosheets based high performance wire type solid-state symmetric supercapacitors. J Power Sources 321:112–119. https://doi.org/10.1016/j.jpowsour.2016.04.116
9. Dalila NR, Arshad MK, Gopinath SCB et al (2019) Biosensors and Bioelectronics Current and future envision on developing biosensors aided by 2D molybdenum disulfide (MoS 2) productions. Biosens Bioelectron 132:248–264. https://doi.org/10.1016/j.bios.2019.03.005
10. Dickinson RG, Pauling L (1923) The crystal structure of molybdenite. J Am Chem Soc 45:1466–1471. https://doi.org/10.1021/ja01659a020
11. Zhang D, Sun Y, Li P, Zhang Y (2016) Facile fabrication of MoS2-modified SnO2 hybrid nanocomposite for ultrasensitive humidity sensing. ACS Appl Mater Interfaces 8:14142–14149. https://doi.org/10.1021/acsami.6b02206
12. Joensen P, Frindt RF, Morrison SR (1986) Single-layer MoS2. Mater Res Bull 21:457–461. https://doi.org/10.1016/0025-5408(86)90011-5
13. Parlak O, İncel A, Uzun L, Turner APF, Tiwari A (2017) Structuring Au nanoparticles on two-dimensional MoS2nanosheets for electrochemical glucose biosensors. Biosens Bioelectron 89:545–550. https://doi.org/10.1016/j.bios.2016.03.024
14. Sun H, Wu S, Zhou X, et al (2019) Electrochemical sandwich immunoassay for insulin detection based on the use of gold nanoparticle-modified MoS2 nanosheets and the hybridization chain reaction. Microchim Acta 186: https://doi.org/10.1007/s00604-018-3124-8
15. Vinita NNR, Prakash R (2018) One step synthesis of AuNPs@MoS2-QDs composite as a robust peroxidase- mimetic for instant unaided eye detection of glucose in serum, saliva and tear. Sensors Actuators B Chem 263:109–119. https://doi.org/10.1016/j.snb.2018.02.085
16. Singha SS, Mondal S, Bhattacharya TS, Das L, Sen K, Satpati B, Das K, Singha A (2018) Au nanoparticles functionalized 3D-MoS 2 nanoflower: an efficient SERS matrix for biomolecule sensing. Biosens Bioelectron 119:10–17. https://doi.org/10.1016/j.bios.2018.07.061
17. Zhang P, Lu X, Huang Y, Deng J, Zhang L, Ding F, Su Z, Wei G, Schmidt OG (2015) MoS2 nanosheets decorated with gold nanoparticles for rechargeable Li-O2 batteries. J Mater Chem A 3: 14562–14566. https://doi.org/10.1039/c5ta02945g
18. Zhang H, Zhang W, Gao X, Man P, Sun Y, Liu C, Li Z, Xu YY, Man B, Yang C (2019) Formation of the AuNPs/GO@MoS2/AuNPs nanostructures for the SERS application. Sensors Actuators B Chem 282:809–817. https://doi.org/10.1016/j.snb.2018.10.095
19. Cao X (2014) Ultra-sensitive electrochemical DNA biosensor based on signal amplification using gold nanoparticles modified with molybdenum disulfide, graphene and horseradish peroxidase. Microchim Acta 181:1133–1141. https://doi.org/10.1007/s00604-014-1301-y
20. Sang F, Zhang X, Liu J, Yin S, Zhang Z (2019) A label-free hairpin aptamer probe for colorimetric detection of adenosine triphosphate based on the anti-aggregation of gold nanoparticles. Spectrochim Acta - Part A Mol Biomol Spectrosc 217:122–127. https://doi.org/10.1016/j.saa.2019.03.081
21. Shi Y, Huang JK, Jin L, Hsu YT, Yu SF, Li LJ, Yang HY (2013) Selective decoration of au nanoparticles on monolayer MoS 2 single crystals. Sci Rep 3:1–7. https://doi.org/10.1038/srep01839
22. Xu Q, Jia H, Duan X, Lu L, Tian Q, Chen S, Xu J, Jiang F (2020) Label-free electrochemical immunosensor for the detection of prostate specific antigen based three-dimensional Au nanoparticles/MoS2-graphene aerogels composite. Inorg Chem Commun 119: 108122. https://doi.org/10.1016/j.inoche.2020.108122
23. Ma G, Xu H, Wu M, et al (2019) A hybrid composed of MoS2, reduced graphene oxide and gold nanoparticles for voltammetric determination of hydroquinone, catechol, and resorcinol. Microchim Acta 186:. https://doi.org/10.1007/s00604-019-3771-4
24. Vilian ATE, Dinesh B, Kang SM, Krishnan UM, Huh YS, Han YK (2019) Recent advances in molybdenum disulfide-based electrode materials for electroanalytical applications Microchim Acta 186:. https://doi.org/10.1007/s00604-019-3287-y
25. Novoselov KS, Geim AK, Morozov S V, et al (2004) Electric field effect in atomically thin carbon films. Science (80-) 306:666–669. https://doi.org/10.1038/nmat1849
26. Radisavljevic B, Radenovic A, Brivio J, Giacometti V, Kis A (2011) Single-layer MoS2 transistors. Nat Nanotechnol 6:147–150. https://doi.org/10.1038/nnano.2010.279
27. Sarkar D, Liu W, Xie X, Anselmo AC, Mitragotri S, Banerjee K (2014) MoS2 field-effect transistor for next-generation label-free biosensors. ACS Nano 8:3992–4003. https://doi.org/10.1021/nn5009148
28. Kalantar-zadeh K, Ou JZ (2016) Biosensors based on two-dimensional MoS2. ACS Sensors 1:5–16. https://doi.org/10.1021/acssensors.5b00142
29. Fathil MFM, Arshad MK, Ruslinda AR et al (2017) Sensors and actuators B : chemical substrate-gate coupling in ZnO-FET biosensor for cardiac troponin I detection. Sensors Actuators B Chem 242: 1142–1154. https://doi.org/10.1016/j.snb.2016.09.131
30. Lee J, Dak P, Lee Y, Park H, Choi W, Alam MA, Kim S (2015) Two-dimensional layered MoS2 biosensors enable highly sensitive

detection of biomolecules. Sci Rep 4:7352. https://doi.org/10.1038/srep07352
31. Taniselass S, Arshad MKM, Gopinath SCB (2019) Graphene-based electrochemical biosensors for monitoring noncommunicable disease biomarkers. Biosens Bioelectron 130: 276–292. https://doi.org/10.1016/j.bios.2019.01.047
32. Miralrio A, Rangel Cortes E, Castro M (2018) Electronic properties and enhanced reactivity of MoS 2 monolayers with substitutional gold atoms embedded into sulfur vacancies. Appl Surf Sci 455: 758–770. https://doi.org/10.1016/j.apsusc.2018.05.220
33. Wang Y, Zhao G, Zhang Y, Pang X, Cao W, du B, Wei Q (2018) Sandwich-type electrochemical immunosensor for CEA detection based on Ag/MoS2@Fe3O4and an analogous ELISA method with total internal reflection microscopy. Sensors Actuators B Chem 266:561–569. https://doi.org/10.1016/j.snb.2018.03.178
34. Yu H, Zhu H, Dargusch M, Huang Y (2018) A reliable and highly efficient exfoliation method for water-dispersible MoS2nanosheet. J Colloid Interface Sci 514:642–647. https://doi.org/10.1016/j.jcis.2018.01.006
35. Winchester A, Ghosh S, Feng S, Elias AL, Mallouk T, Terrones M, Talapatra S (2014) Electrochemical characterization of liquid phase exfoliated two-dimensional layers of molybdenum disulfide. ACS Appl Mater Interfaces 6:2125–2130. https://doi.org/10.1021/am4051316
36. Yang Y, Liu T, Cheng L, Song G, Liu Z, Chen M (2015) MoS2-based nanoprobes for detection of silver ions in aqueous solutions and bacteria. ACS Appl Mater Interfaces 7:7526–7533. https://doi.org/10.1021/acsami.5b01222
37. Marx M, Nordmann S, Knoch J, Franzen C, Stampfer C, Andrzejewski D, Kümmell T, Bacher G, Heuken M, Kalisch H, Vescan A (2017) Large-area MoS2 deposition via MOVPE. J Cryst Growth 464:100–104. https://doi.org/10.1016/j.jcrysgro.2016.11.020
38. Yang L, Guo S, Li X (2017) Au nanoparticles@MoS2core-shell structures with moderate MoS2coverage for efficient photocatalytic water splitting. J Alloys Compd 706:82–88. https://doi.org/10.1016/j.jallcom.2017.02.240
39. Zhao Y, Pan X, Zhang L, Xu Y, Li C, Wang J, Ou J, Xiu X, Man B, Yang C (2017) Dense AuNP/MoS2 hybrid fabrication on fiber membranes for molecule separation and SERS detection. RSC Adv 7:36516–36524. https://doi.org/10.1039/c7ra05568d
40. Ma H, Shen Z, Ben S (2018) Understanding the exfoliation and dispersion aof MoS2 nanosheets in pure water. J Colloid Interface Sci 517:204–212. https://doi.org/10.1016/j.jcis.2017.11.013
41. Amini M, Ramazani SAA, Faghihi M, Fattahpour S (2017) Preparation of nanostructured and nanosheets of MoS2 oxide using oxidation method. Ultrason Sonochem 39:188–196. https://doi.org/10.1016/j.ultsonch.2017.04.024
42. Merida CS, Le D, Echeverría EM, et al (2017) Gold dispersion and activation on the basal plane of single-layer MoS gold dispersion and activation on the basal plane of single-layer MoS 2. https://doi.org/10.1021/acs.jpcc.7b07632
43. Letchumanan I, Md Arshad MK, Balakrishnan SR, Gopinath SCB (2019) Gold-nanorod enhances dielectric voltammetry detection of c-reactive protein: a predictive strategy for cardiac failure. Biosens Bioelectron 130:40–47. https://doi.org/10.1016/j.bios.2019.01.042
44. Su S, Sun H, Xu F, et al (2013) Highly sensitive and selective determination of dopamine in the presence of ascorbic acid using gold nanoparticles-decorated MoS2 nanosheets modified electrode. 1–7. https://doi.org/10.1002/elan.201300332
45. Kukkar M, Sharma A, Kumar P, Kim KH, Deep A (2016) Application of MoS2 modified screen-printed electrodes for highly sensitive detection of bovine serum albumin. Anal Chim Acta 939: 101–107. https://doi.org/10.1016/j.aca.2016.08.010
46. Gill GN (1971) Properties of CRP. Methods Enzymol 512:376–382
47. Shrivastava A, Gupta V (2011) Methods for the determination of limit of detection and limit of quantitation of the analytical methods. Chronicles Young Sci 2:21. https://doi.org/10.4103/2229-5186.79345
48. Kim K-Y, Chang H, Lee W-D, Cai YF, Chen YJ (2019) The influence of blood glucose meter resistance variation on the performance of a biosensor with a gold-coated circuit board. J Sensors 2019:1–8. https://doi.org/10.1155/2019/5948182
49. Pang P, Teng X, Chen M, Zhang Y, Wang H, Yang C, Yang W, Barrow CJ (2018) Ultrasensitive enzyme-free electrochemical immunosensor for microcystin-LR using molybdenum disulfide/gold nanoclusters nanocomposites as platform and au@Pt core-shell nanoparticles as signal enhancer. Sensors Actuators B Chem 266:400–407. https://doi.org/10.1016/j.snb.2018.03.154
50. Kutova O, Dusheiko M, Klyui NI, Skryshevsky VA (2019) C-reactive protein detection based on ISFET structure with gate dielectric SiO 2 -CeO 2. Microelectron Eng 215:110993. https://doi.org/10.1016/j.mee.2019.110993
51. Lee SH, Choi S, Kwon K, Bae NH, Kwak BS, Cho WC, Lee SJ, Jung HI (2017) A photothermal biosensor for detection of C-reactive protein in human saliva. Sensors Actuators B Chem 246: 471–476. https://doi.org/10.1016/j.snb.2017.01.188
52. Esteban-Fernández De Ávila B, Escamilla-Gómez V, Campuzano S et al (2013) Ultrasensitive amperometric magnetoimmunosensor for human C-reactive protein quantification in serum. Sensors Actuators B Chem 188:212–220. https://doi.org/10.1016/j.snb.2013.07.026